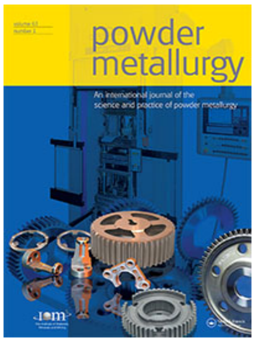

Powder Metallurgy

ISSN: 0032-5899 (Print) 1743-2901 (Online) Journal homepage: https://www.tandfonline.com/loi/ypom20

In-situ VN reinforced powder metallurgy M30 steels prepared from water atomized powers via pressureless sintering

Haixia Sun, Fang Yang, Qian Qin, Biao Zhang, Alex A. Volinsky & Zhimeng Guo

To cite this article: Haixia Sun, Fang Yang, Qian Qin, Biao Zhang, Alex A. Volinsky & Zhimeng Guo (2020) In-situ VN reinforced powder metallurgy M30 steels prepared from water atomized powers via pressureless sintering, Powder Metallurgy, 63:1, 43-53, DOI: 10.1080/00325899.2020.1717075

To link to this article: https://doi.org/10.1080/00325899.2020.1717075

POWDER METALLURGY
2020, VOL. 63, NO. 1, 43–53
https://doi.org/10.1080/00325899.2020.1717075

RESEARCH ARTICLE

In-situ VN reinforced powder metallurgy M30 steels prepared from water atomized powers via pressureless sintering

Haixia Sun[a], Fang Yang[a], Qian Qin[a], Biao Zhang[a], Alex A. Volinsky[b] and Zhimeng Guo[a]

[a]Institute for Advanced Materials and Technology, University of Science and Technology Beijing, Beijing, People's Republic of China;
[b]Department of Mechanical Engineering, University of South Florida, Tampa, FL, USA

ABSTRACT

In this paper, in-situ VN reinforced powder metallurgy high-speed steel was fabricated from water atomised powder via pressureless sintering. During sintering, N would replace C to react with V, resulting in the formation of in-situ VN phase. According to the first-principles calculations, the formation energy of VN was − 9.45 eV while that of VC was − 9.08 eV. The relative density of as-sintered samples reached up to 99%. Homogeneous microstructure and fine reinforced phases were obtained. Ultrafine VN phase (0.5 μm) was uniformly distributed in the matrix. As a result, the mechanical properties were improved. The optimal mechanical performance was obtained in the sample with 1.0 wt.% C addition. The hardness, bend strength and impact energy were 65 HRC, 3011 MPa and 18–22 J, respectively. Besides, the sintering window significantly increased from ∼10 to 30∼50°C.

ARTICLE HISTORY
Received 7 October 2019
Revised 5 January 2020
Accepted 9 January 2020

KEYWORDS
High-speed steel; pressureless sintering; VN; microstructure; mechanical performance

1. Introduction

Owing to their excellent strength, toughness and hardness, tool steels are widely used in cutting tools and wear parts. Among tool steels, high-speed steel (HSS) is one of the most common kinds with special microstructure and excellent properties. In terms of the microstructure, fine carbides are uniformly distributed in the steel matrix. Thereinto, the carbides characteristics, such as particle size, distribution, structure and interface with the matrix play an important role in determining the microstructure and mechanical properties of the HSS.

It is known that the carbides' morphology of HSS depends on the fabrication process [1–3]. Besides, the carbides structure and interface character are closely related to the phase composition. Carbide, particularly primary carbide, is crucial, which significantly affects the strength, hardness, and processability. The primary carbide mainly consists of tungsten and molybdenum-rich M_6C, vanadium-rich MC, and even M_2C with a granular or irregular shape in the cast HSS [4–6]. Generally, the preparation process mainly includes casting and powder metallurgy (PM). The M_2C is a representative carbide in cast steels with relatively large and bulkier particle size. In order to refine the coarse carbides formed during the casting process, a large amount of forging deformation is required, resulting in the strip-shaped microstructure which causes the anisotropy properties [7]. The PM process can solve the problems of coarse primary carbide and material anisotropy.

In general, the PM process for preparing HSS mainly includes hot isostatic pressing (HIP), pressureless sintering, and injection moulding. During the HIP process, gas atomised HSS powder and steel capsule are employed [8]. Besides, the requirements for HSS powder quality are very stringent and the manufacturing process is relatively complex. These greatly restrict the development of PM HSS. It is well known that gas atomised powder is spherical with extremely low oxygen content, while water atomised powder is mainly irregular with relatively high oxygen content. During the gas atomisation process, the heat exchange of the particles in the gas environment is slow, resulting in a low particle cooling rate. In such case, the particle droplets automatically shrink into the sphere. In the contrary, because of the chilling effect of water on the atomised droplets, the particles solidify into alloy powder instantaneously, resulting in the less surface tension of water atomised powder with an irregular shape. Therefore, gas atomised HSS powder is more suitable for HIP sintering with low oxygen content. As to pressureless sintering, it is a promising method to produce HSS using water atomised powder. Generally, water atomised HSS powder is mainly adopted, which can be sintered to nearly full densification. Besides, the sintering is carried out under vacuum or nitrogen atmosphere. At present, the densification is achieved by supersolidus liquid phase sintering (SLPS) [9,10]. In such case, densification and microstructural control are correlated with pseudobinary phase diagrams. The optimal sintering takes place on heating to a four phase austenite + M_6C

CONTACT Fang Yang yangfang@ustb.edu.cn Institute for Advanced Materials and Technology, University of Science and Technology Beijing, Beijing 100083, People's Republic of China; Zhimeng Guo zmguo@ustb.edu.cn Institute for Advanced Materials and Technology, University of Science and Technology Beijing, Beijing 100083, People's Republic of China

+ MC + liquid region. When the solidus-liquidus interval is wider and the slope of the solidus line is deeper, the sintereability is superior. Therefore, many efforts have been reported focusing on the preparation of HSS with water atomised powders. The studies on how to achieve pressureless sintering of HSS have received extensive attention due to their low cost [11,12]. Giménez et.al studied the microstructure characteristics of HSS fabricated by HIP, vacuum sintering, and nitrogen sintering [13]. After sintering under different nitrogen partial pressure conditions, there was no big difference in the M_6C phase, except for the MC phase. The transformation of stiffer MN phase from the MC phase occurred, which had a beneficial effect on toughness and strength of HSS. As a drawback, the reaction was accompanied by the formation of the M_3C network carbides, which was detrimental for achieving good performance. A similar report was presented in Ref. [14]. Although fine and spherical MN phase was obtained in the V-containing HSS, the M_3C network carbides and coarse M_6C carbides were also formed, resulting in the destruction of isotropic properties [14]. Although TiC, NbC, and MnS reinforced PM HSS have been studied [15–17], there is no related reports on preparing MN-reinforced HSS with isotropic properties.

In this paper, in-situ VN reinforced PM HSS was prepared by pressureless sintering under the nitrogen atmosphere. Among commonly used pressureless sintering processes, nitrogen sintering was widely employed in the preparation of metal and ceramic parts [18–20]. As opposed to the common pressureless sintering process via adding graphite to balance the carbon content, this study was designed to decrease the carbon content in the V-containing HSS. Despite that, the PM HSS with VN strengthening possessed excellent performance. The carbon effects and sintering behaviour in the PM HSS were studied. Besides, the microstructure, elemental distribution and phase composition of the VN reinforced phase were investigated. Accordingly, the hardness, bend strength and impact energy were measured. Based on the analysis of phase formation energy and standard Gibbs free energy, the formation mechanism of carbides and nitrides in the HSS was also clarified.

2. Experimental procedures

2.1. Processing

The raw material was water atomisation HSS powder with a nominal composition of 4.33Cr–6.30W–4.96Mo–2.97V–8.72Co–xC-bal. Fe ($x = 0.8$, 1, and 1.2 wt.%). The powder was purchased from the Antai Technology Co., Ltd., with an average powder particle size of 10 μm. The preparation process comprised the following steps. First, the powder was compressed by the hydraulic press with a pressure of 700 MPa. Then, the compacts were pressureless sintered at different temperatures under nitrogen atmosphere with a heating rate of 5°C min^{-1}. The sintering temperature was chosen according to the study reported in Ref. [13], and the gas flow rate was 300 mL min^{-1}. Subsequently, furnace cooling to room temperature was performed. Lastly, heat treatment was carried out as follows: austenitising at 1150°C for 10–20 min, oil quenching, and triple tempering at 500–600°C for 1–2 h. For comparison, traditional M30 samples were also prepared by vacuum sintering under 10^{-1}–10^{-3} Pa. The heat treatment parameters were the same as before.

2.2. Characterisation

The density of the as-sintered samples was measured by the Archimedes method. Five samples for each processing condition were employed to confirm repeatability. Mechanical properties were evaluated in terms of the hardness, bend strength, and room temperature impact tests. The hardness of the samples after heat treatment was determined by a TH320 Rockwell hardness tester. The bend strength was measured by the three-point bending test with an electronic universal testing machine (CMT6140) at a loading rate of 0.5 mm s^{-1}. The size of the tested samples was 35 mm × 5 mm × 5 mm with a span of 30 mm. Besides, the impact energy was measured by the non-notch impact test using a CMT4105 electronic universal testing machine, in which the sample size was 55 mm × 10 mm × 10 mm. The abrasive wear resistance test was carried out under load of 30 N for 120 s, using a ML-100 wear testing machine. Abrasive was 600# SiC sandpaper and the sample size was φ10 mm*15 mm. The oxygen and nitrogen contents were measured using a pulsed infrared thermal conductivity oxygen-nitrogen analyser (ONH-2000). The phase formation energy was calculated by the norm-conserving pseudo-potential method (CASTEP). Powder morphology, microstructure, fracture and worn surface were analysed using a scanning electron microscopy (SEM, Philips LEO-1450) equipped with energy-dispersive spectroscopy (EDS, Model JEOL, JEOL Ltd., Tokyo, Japan). Element distribution was observed by a field emission scanning electron microscope (FESEM, Zeiss Supra55). Phase identification was analysed using a transmission electron microscope (TEM, Tecnai G2 F30 S-TWIN) operating at 300 kV. Phase analysis was carried out using an X-ray diffraction (XRD, Shimadzu XRD-6000, Cu Kα target, 40 kV and 40 mA).

3. Results and discussion

3.1. Densification

The morphology of raw HSS powders is shown in Figure 1. The powders were irregular and ellipsoid.

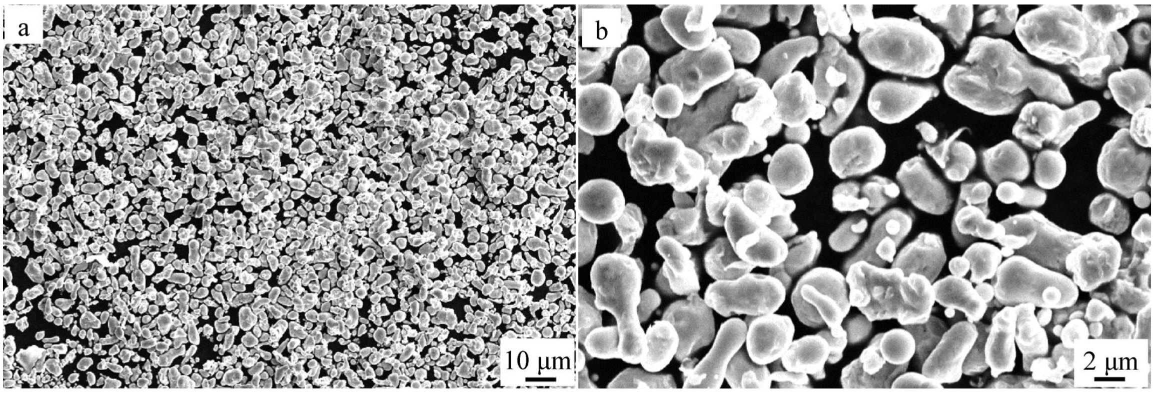

Figure 1. SEM images of raw HSS powder at: (a) low, and (b) high magnification.

Fine powder (~10 μm) was employed to ensure the sinterability in the pressureless sintering process. Owing to the subtle distinctions in powder composition, the four kinds of green compacts were sintered at different temperatures to guarantee the as-sintered samples obtaining the optimal mechanical performance. Accordingly, the temperature parameters and sintering behaviour of different samples are summarised in Table 1. As reported in Ref. [13], the optimal sintering temperature (OST) is the lowest sintering temperature for achieving the relative density of above 98%. The sintering window (SW) is corresponding to the temperature interval between the OST and the incipient melting temperature of the M_6C phase. The higher the SW value, the lower the probability of grain growth caused by local overheating. As presented in Table 1, with the carbon content decreasing, the density of the samples sintered under nitrogen decreased, while the OST increased. The relative densities of all samples were over 98%. Besides, the relative density of the M30 sample was about 99%, which was approximately equal to the value of the NM30-2 sample. However, it was worth noting that the SW values of the NM30-2 and NM30-3 samples were obviously higher than the M30 sample.

3.2. Microstructure and properties

The microstructures of different as-sintered samples are shown in Figure 2. A typical HSS microstructure with reinforced carbide or nitride phases distributed in the matrix was observed. The dark grey phase was corresponding to the matrix phase. In the M30 sample, two kinds of reinforced carbide phases were obtained, as shown in Figure 2(d). According to the EDS results, the white phase was corresponding to the M_6C carbide, enriched with tungsten and molybdenum elements. The light grey phase was the V-rich MC carbide. These results were consistent with the literatures [21,22]. Different from the M30 sample, there was another black phase formed in the samples sintered under nitrogen, as shown in Figure 2(a–c). It was a hard phase enriched with V and N elements. As shown in Figure 2, the average particle size of carbides was about 1–2 μm, except for the NM30-1 sample. Lath-shaped carbides were also found in Figure 2(a). It was worth noting that the formed nitride phases were ultrafine, less than 1 μm. The microstructure of samples sintered under nitrogen was distinctly different from the common PM HSS [23].

To further confirm the phase composition and crystal structure, FESEM, XRD and TEM investigations were performed. The element distribution of Fe, V, Mo, W, Co, C, and N elements is presented in Figures 3 and 4. Fe and Co were thought to be dominant in the matrix while C was distributed uniformly in the matrix and the reinforced phase. It can be observed that N and V were mainly precipitated in the black region, corresponding to the nitride phases. As for the N-free bright phase, it mainly consisted of W and Mo elements. The distribution of W and Mo elements were completely overlapped. Therefore, both the M_6C and nitride phases were observed in all NM30 samples, and no MC phase was detected. As reported in Ref. [13], the change in the sintering process would affect the formation of the MC phase when the HSS samples were sintered under nitrogen. The formation mechanism would be discussed in further detail.

Table 1. C, N and O contents and density for HSS samples sintered at optimum sintering temperatures (OST).

Sample	Condition	C (wt.%)	O (wt.%)	N (wt.%)	Density (g cm^{-3})	Relative Density (%)	OST (°C)	SW (°C)
NM30-1	Nitrogen	1.2	0.013 ± 0.001	0.75 ± 0.01	8.02 ± 0.01	99.75	1180	<5
NM30-2		1.0	0.015 ± 0.001	0.82 ± 0.01	7.98 ± 0.01	99.25	1210	30~50
NM30-3		0.8	0.018 ± 0.001	0.92 ± 0.01	7.89 ± 0.01	98.13	1250	>50
M30	Vacuum	1.2	0.012 ± 0.001	0.02 ± 0.01	7.96 ± 0.01	99.00	1230	≈10

Note: Sintering windows (SW) is reported in Ref. [13].

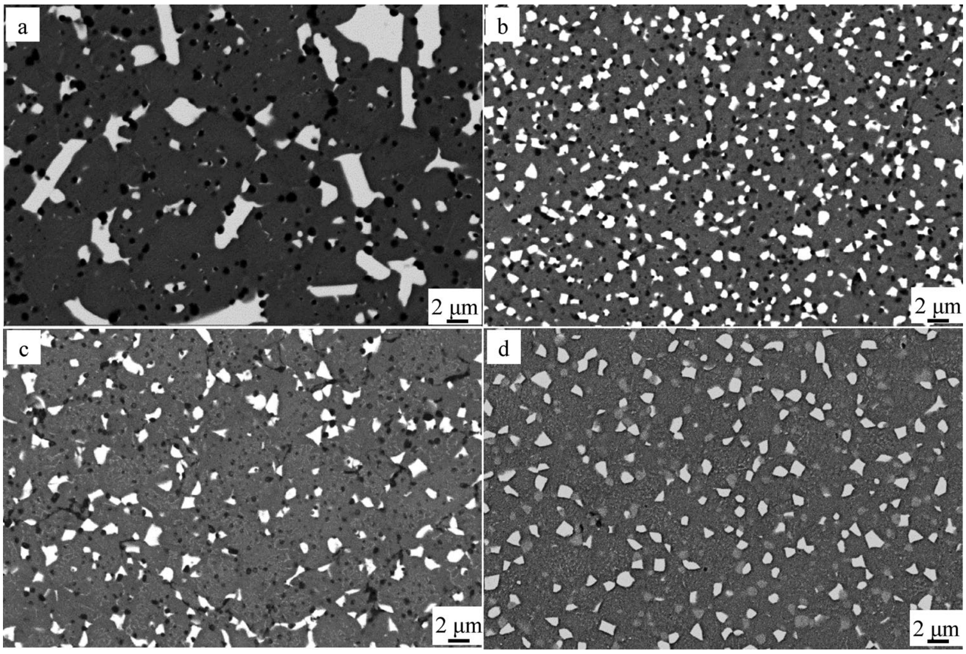

Figure 2. Microstructures of different as-sintered HSS samples: (a) NM30-1, (b) NM30-2, (c) NM30-3, and (d) M30.

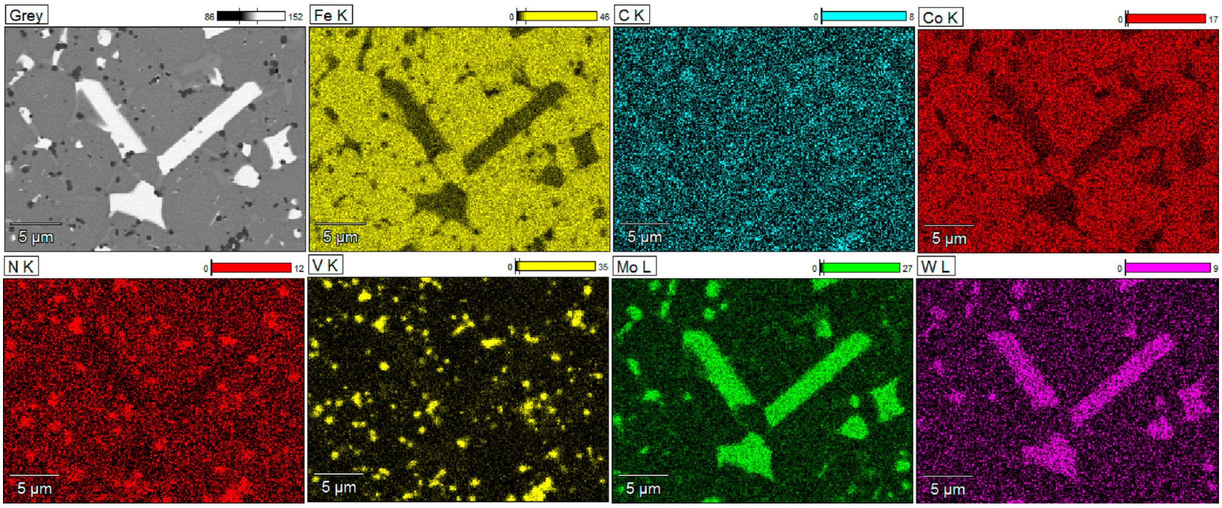

Figure 3. Fe, V, Mo, W, Co, C and N elements distribution in the NM30-1 HSS sample.

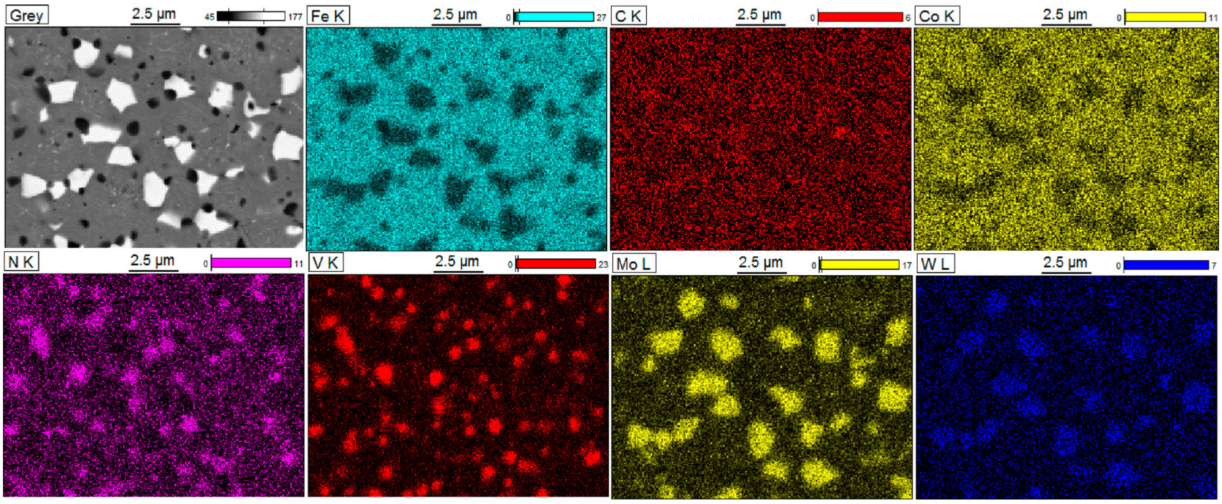

Figure 4. Fe, V, Mo, W, Co, C and N elements distribution in the NM30-2 HSS sample.

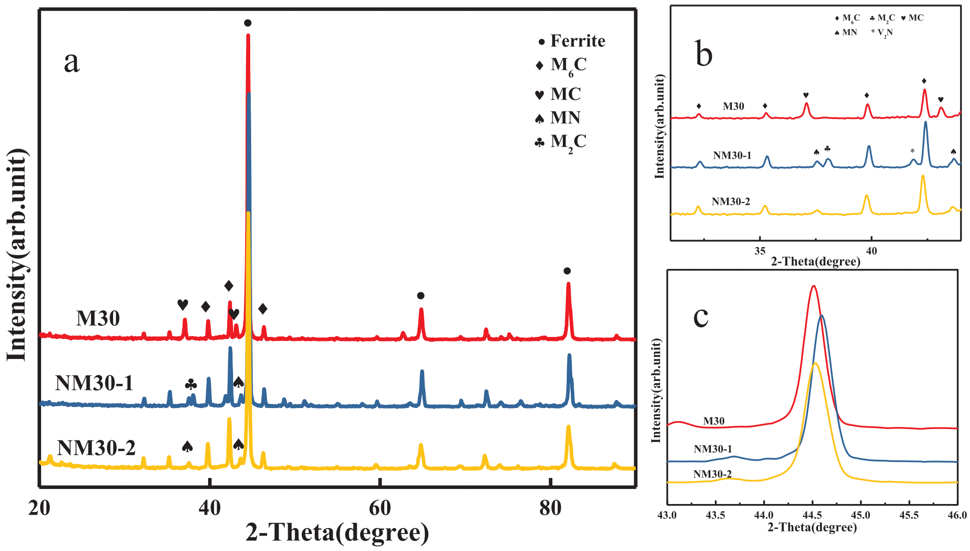

Figure 5. XRD patterns of the as-sintered HSS samples detected at: (a) 20–90°, (b) 31–44°, and (c) 43–46°.

The phase composition was characterised by XRD, as shown in Figure 5. Overall speaking, M_6C and MC were detected in the M30 sample, while ferrite, M_6C, and MN were detected in the NM30 sample. It was worth noting that M_2C was also observed in the NM30-1 sample, which would be harmful for the mechanical performance. The only difference between the NM30-1 and NM30-2 samples was the carbon content. Compared with the NM30-2 sample, an extra 0.2 wt.% C was introduced into the NM30-1 sample. It can be inferred that the carbon content should be strictly controlled. To further analyse the phases characteristics, the peak details were detected from 31° to 44° and 43° to 46°, as shown in Figure 5(b,c). Face-centred cubic MC phase was only observed in the M30 sample. The MN phase was only found in the samples sintered in nitrogen. No impurity phases, like M_2C and V_2N, were detected in the NM30-2 sample compared with the NM30-1 sample. For the MC and MN phases, nitrogen and carbon atoms were occupied in the octahedral spaces of the vanadium atom. Thereinto, the radius of the nitrogen atom (0.071 nm) was smaller than the carbon atom (0.77 nm). As to the ferrite, there was no peak position shift between the M30 and NM30-2 samples. However, for the NM30-1 sample, the peak of ferrite shifted to a higher diffraction angle. This implied that there were atoms dissolved in the matrix, leading to the decreasing of lattice spacing. It can be inferred that when sintered under nitrogen, N would react with V to form the VN phase. Comparing the M30 and NM30-1 samples, although the carbon content was the same, V atoms were occupied by N atoms, leading to an excess carbon content. According to the XRD analysis, part of the excess C would dissolve into the matrix, resulting in the peak shift, and another part would form the M_2C phase. Therefore, the lath-shaped carbides, shown in Figure 2(a), might be the M_2C phase enriched with molybdenum and tungsten, which were similar to the carbides in cast HSS [24,25].

The reinforced phase was further identified by TEM analysis, as presented in Figure 6. From EDS results shown in Figure 6(a,b), region 'A' was the carbide phase enriched with W and Mo, while region 'B' was the nitride phase enriched with V. The corresponding SAED patterns are shown in Figure 6(d,e). The SAED pattern of region 'A' was indexed as cubic M_6C phase with $a = 1.114$ nm. The zone axis was [001]. Another SAED pattern revealed that region 'B' was corresponding to face-centred cubic VN phase with $a = 0.414$ nm. The zone axis was also identified as [001]. Besides, the grain size of the M_6C phase was about 1 μm. However, the grain size of the VN phase was much smaller, about 0.5 μm. Fine VN reinforced phase was formed during sintering, which may enhance the mechanical performance.

Accordingly, the hardness, bend strength and impact energy of different samples are listed in Table 2. The hardness, bend strength and impact energy of the M30 sample were 65 HRC, 2962 MPa and 15–20 J, respectively. The optimal mechanical performance was obtained in the NM30-2 sample. There was no big difference in hardness. However, the bend strength of the NM30-2 sample was up to 3011 MPa, which was 50% higher than that of the NM30-1 sample. The impact energy increased from 2–5 to 18–22 J. Figure 7 presents the mechanical properties of different PM HSS samples. Comparing the M30 and NM30-2 samples, there was an obvious yield plateau observed in NM30-2 sample, just like the green mark in Figure 7. As a result, the strain value of NM30-2 was much larger than M30, indicating that fine VN phase could contribute to improving the plasticity of HSS parts. It can be inferred that the failure of tool tipping would be significantly reduced, resulting in a prolonged service life of HSS. The mechanical

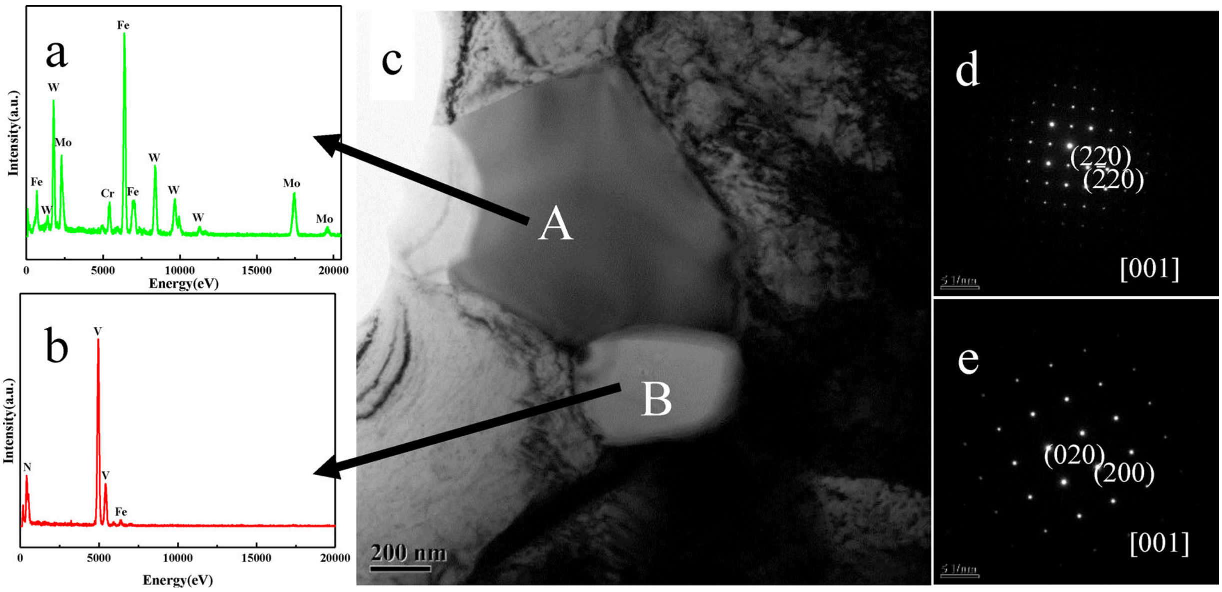

Figure 6. EDS analysis of region (a) A, (b) B, (c) TEM image and SAED patterns of region (d) A, and (e) B in sample NM30-2.

properties were strongly related to the microstructure. Therefore, the performance enhancement was mainly attributed to the formation of fine VN reinforced phase.

The fracture morphology of different HSS samples is shown in Figure 8. The fracture mainly occurred along the bonding interface between the matrix and the reinforced phases. It can be clearly observed that there were larger reinforced phases in the NM30-1 sample, indicated by the white arrow in Figure 8(d). These might be the lath-shaped carbides. The large block M_6C or M_2C carbides caused considerably high stress concentration in the surrounding area, leading to early bend or fracture. Hence, the bend strength and impact energy of the NM30-1 sample were much lower. In contrast, the NM30-2 sample had homogeneous microstructure with fine carbides and nitrides evenly distributed in the matrix, which was beneficial for withstanding much larger bend and impact forces. Therefore, the mechanical performance of the NM30-2 sample was much higher than NM30-1.

Table 2. Mechanical properties of PM HSS.

	Carbon content (wt.%)	Hardness (HRC)	Bend strength (MPa)	Impact energy (J)
NM30-1	1.2	68 ± 1.3	2097 ± 45	2~5
NM30-2	1.0	65 ± 1.5	3011 ± 50	18~22
NM30-3	0.8	60 ± 1.4	–	–
M30	1.2	65 ± 1.5	2962 ± 50	15~20

Moreover, the wear resistance analysis was also carried out, as shown in Figure 9. It can be seen that NM30-1 sample showed the worst wear resistance. Obvious plough scratch was observed in Figure 9(a). The grooves were relatively deeper. In contrast, the wear resistance of NM30-3 sample was much better than that of NM30-1 sample. It might be attributed to fine hard particles existed in the matrix. Overall, NM30-2 and M30 samples had the best wear resistance. The worn surface for NM30-2 sample was similar to M30 sample, as shown in Figure 9(f,h). As shown in Figure 2, the carbides and nitrides in NM30-2 and M30 samples were fine and homogeneous, and the particle

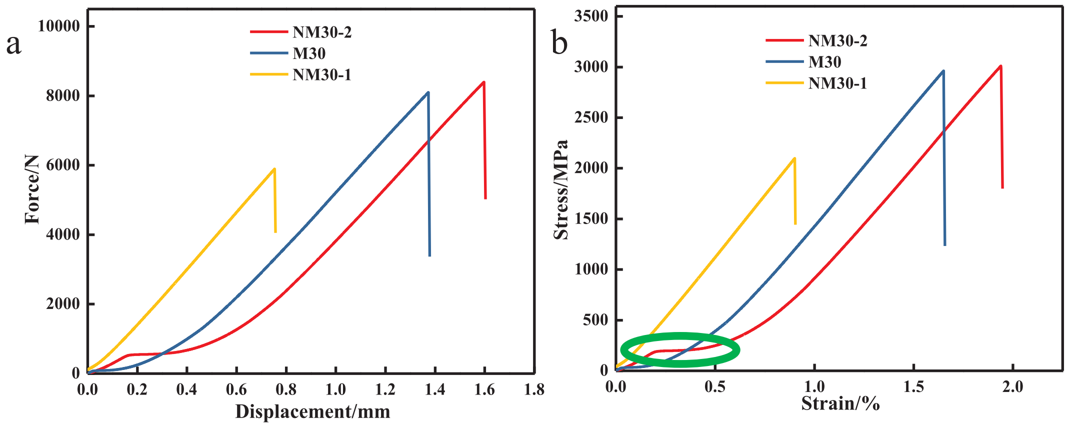

Figure 7. (a) Force-displacement curve, and (b) stress–strain curve of PM HSS samples.

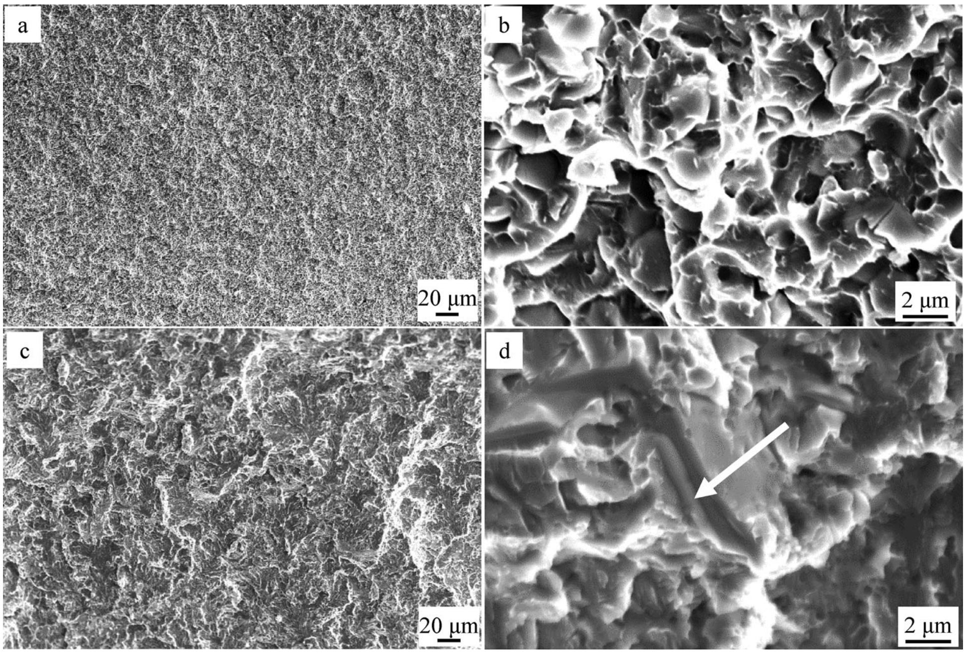

Figure 8. Fracture morphology of different HSS samples: (a, b) NM30-2, (c, d) NM30-1.

spacing was relatively small, resulting in the obtainment of better wear resistance. Besides, according to the wear test shown in Figure 9, VC and VN should have similar wear resistance.

3.3. Formation mechanism

To understand the formation mechanism, the standard reaction Gibbs free energy of VN and VC was calculated, as shown in Figure 10. The reaction can be presented as Equation (1). At 1210°C, the ΔG values of VC and VN were −85.736 and −471.58 J, respectively. The ΔG of VN was much more negative than VC, indicating that the formation of the VN phase had a higher tendency. As mentioned in Table 1, the sintering temperature of the HSS samples was about 1200°C. Therefore, nitrogen gas would react with V to form in-situ VN phase during sintering.

$$V + C(N) = VC(N) \tag{1}$$

Furthermore, the first principles calculations were employed to calculate the phase formation energy. The crystal models of VC/VN were built, as shown in Figure 11(a). The VC/VN phase had a simple face-centred cubic structure. Accordingly, the formation energy of VC and VN phase was calculated, as shown in Figure 11(b). The lower the formation energy, the

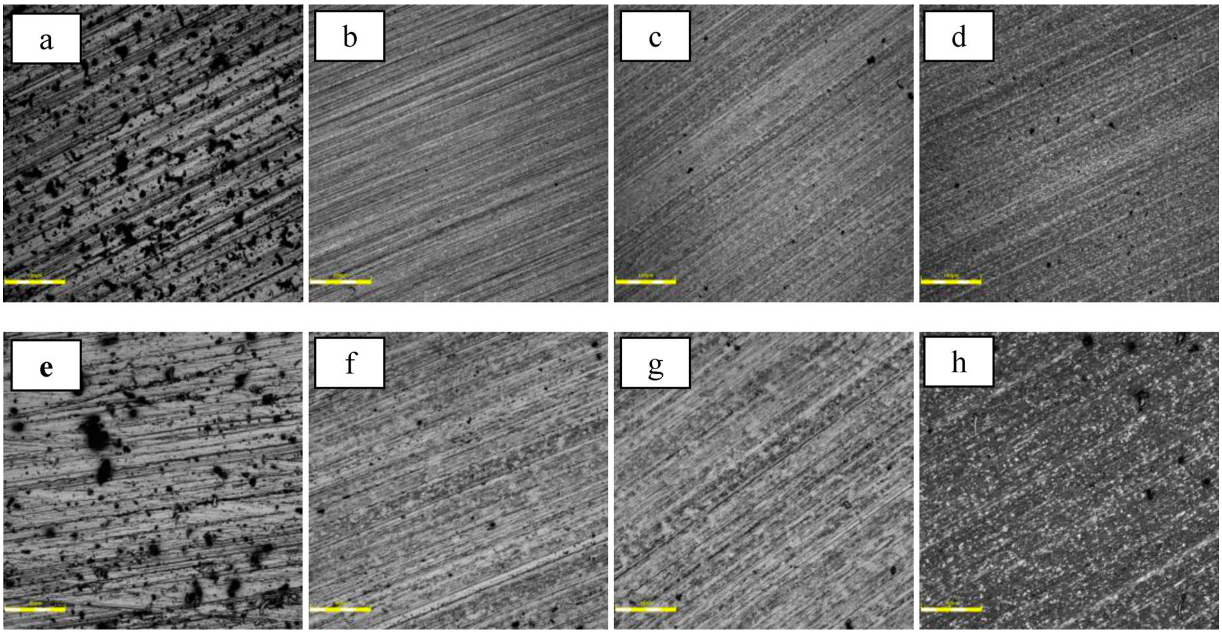

Figure 9. SEM images of worn tools: (a, e) NM30-1, (b, f) NM30-2, (c, g) NM30-3, and (d, h) M30.

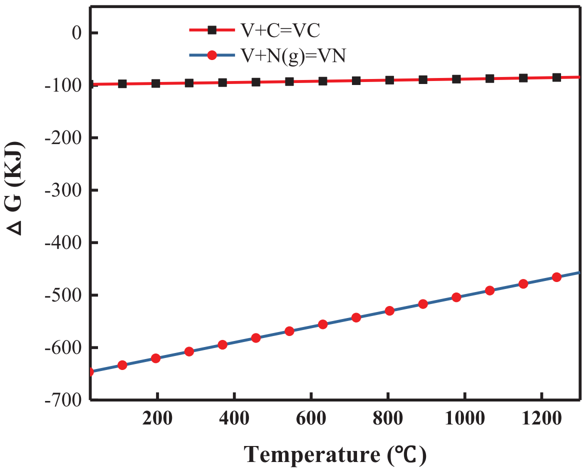

Figure 10. Standard Gibbs free energy change (ΔG°) as a function of temperature.

more stable the phase was, and correspondingly, the higher its formation tendency. It can be observed that with the N content increase in the VC phase, the formation energy value was more negative. The values of the VC and VN phase were −9.08125 and −9.44895 eV, respectively. This further proved the stability of the VN phase was higher than VC, which was consistent with the result shown in Figure 10. Compared with VC, VN had more negative ΔG and phase formation energy. During the nitrogen sintering process, in-situ VN reinforced phase would form and its particle size was ultrafine.

The driving force of sintering was the reduction of free energy (ΔZ) of the sintering system. As shown in Table 1, the density of the NM30-2 sample was 7.98 g cm^{-3}, which was slightly higher than the M30 sample. It can be inferred that the ΔZ value would go down more when forming VN rather than VC, leading to the density further being closer to the theoretical density. Besides, nitrogen gas provided an activated sintering atmosphere for V-containing HSS. General speaking, in the final stage of sintering, the elimination of pores depended on the difference between residual gas pressure and surface tensile stress. As presented in Equation (2), the P_s represented the force to promote densification sintering. Thereinto, the P_v was the residual gas pressure in the pores, while $\frac{2\gamma}{\rho}$ was corresponding to the surface tensile stress. If the $\frac{2\gamma}{\rho}$ value was larger than P_v, the pores can keep shrinking. In contrast, if the gas remained in the sample, the P_v value would be large enough to exceed the $\frac{2\gamma}{\rho}$, resulting in the stop of sintering shrinkage and the existence of pores [26]. When sintered under nitrogen, the residual gas was nitrogen, which would diffuse into the powders to form nitride. As a result, the sintering driving force significantly improved. Therefore, the nitrogen activated sintering was a promising method to prepare full density V-containing HSS parts.

$$P_s = \frac{2\gamma}{\rho} - P_v \tag{2}$$

3.4. Discussion

The above results indicated that the in-situ formed nitride opened new possibilities for fabricating HSS with high performance. The sintering densification was decided by the sintering neck forming and pore eliminating. Fine HSS powder (10 μm) had a relatively large surface area and energy, resulting in the obtainment of high relative density (>98%) when pressureless sintered under vacuum or nitrogen atmosphere. When sintered under nitrogen, the formation energy of VN was more negative, resulting in the formation of in-situ fine VN phase instead of VC phase. Besides, nitrogen effect on improving the sinterability of HSS can be described in terms of the enlargement of the austenite + M_6C + MC + liquid region. In the V-containing HSS, the relationship between C content and N absorption played an important role in controlling densification sintering. When sintering under nitrogen, VN was formed instead of VC. In such case, free carbon was available to dissolve into the matrix, thus decreasing the solidus temperature. Furthermore, as the SW value of the NM30-2 sample greatly increased, the

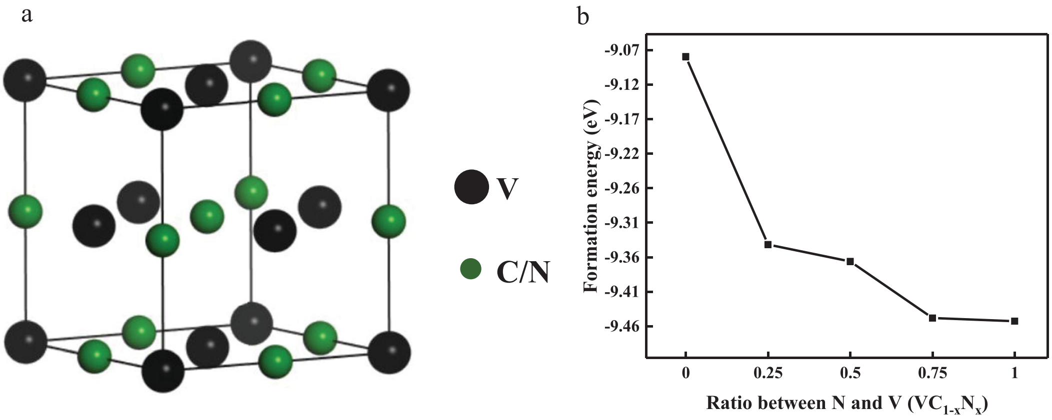

Figure 11. (a) Crystal structure of $VC_{1-x}N_x$ ($x = 0$–1), and (b) corresponding formation energy change as a function of nitrogen atomic percent.

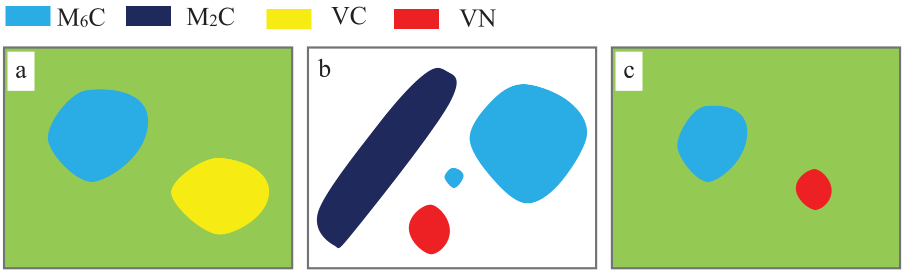

Figure 12. Schematics of microstructure development in HSS: (a) carbon balance state, (b) carbon imbalance state, (c) new carbon–nitrogen balance state.

difficulty in controlling the sintering process significantly reduced, which would make industrialised production more convenient and reduce the requirements for production equipment.

The composition of the reinforced phase was closely related to the carbon content. As the carbon content decreased, the M_2C phase gradually disappeared and the M_6C amount slightly reduced. When the carbon content was 1.0 wt.%, the reinforced phases were just M_6C and MN. Homogenous microstructure was obtained with fine M_6C (1 µm) and ultrafine MN phase (0.5 µm) distributed in the matrix. According to TEM analysis, M_6C phase had a complex cubic structure. There were 96 metal atoms (mainly Fe, W, and Mo) and 16 carbon atoms in the unit cell. Rather, MN phase possessed a simple face-centred cubic structure, in which M atoms occupied the top and centre sites, while N atoms occupied the octahedral gaps. Because the radius of nitrogen atom (0.071 nm) was less than the carbon atom (0.077 nm), the value of R_n/R_m was smaller than R_c/R_m. Therefore, the formed MN was more stable than the MC [27].

As shown in Table 1, there was an obvious difference on the C and N contents in the as-sintered HSS samples. The transformation of the reinforced phase in HSS is sketched in Figure 12. Figure 12(a) presents a carbon balance state in HSS when sintered under vacuum. When sintered under nitrogen, if the HSS system was in the carbon imbalance state, lath-shaped M_2C and M_6C were formed with larger particle size. For the M30 sample, the balanced carbon content was 1.2 wt.%. Although the carbon content was the same in the NM30-1 sample, the formation of the VN phase would lead to an excess of carbon. This was attributed to the lower formation energy of VN. Therefore, the carbon content should be properly decreased, just like the NM30-2 sample. A carbon–nitrogen balance state was essential for obtaining high-performance HSS.

This new HSS was designed with lower carbon content to achieve the balance between carbon and nitrogen. During sintering, nitrogen diffused into the matrix to take part in the reaction of nitride formation. The nitride was predominantly the VN phase, which had lower standard reaction Gibbs free energy and more negative phase formation energy. Compared with VC, in-situ VN was smaller and more stable, leading to higher strength and toughness. Therefore, the optimal mechanical performance was obtained in the NM30-2 sample. The hardness, bend strength and impact energy were 65 HRC, 3011 MPa and 18∼22 J, respectively.

It is well known that these materials do not fracture in a classical Griffith manner, but have an intermediate crack growth stage in monotonic fracture, and also show *R*-curve behaviour [28]. Typical plastic zone sizes can be calculated from the relationship: radius of the plastic zone $R_p = 1/6\pi[K_{IC}/\sigma_{yld}]^2$, where K_{IC} is the fracture toughness, σ_{yld} is the yield stress. In general, $\sigma_{yld} \approx (3.27H_m)MPa$, and H_m is the micro-hardness of the steel matrix [15]. In simple terms, R_p would increase with the increase of K_{IC}. From the bend strength curve shown in Figure 7, the intermediate crack growth stage of NM30-2 sample was more slow, indicating that it might potentially have a high fracture toughness. According to the radius of plastic zone, it could be inferred that NM30-2 sample may have larger plastic zone. However, this need to be investigated further and in depth. In our future research, the fracture behaviour and cutting tool performance of VN reinforced HSS would be studied in detail.

4. Conclusions

In this study, in-situ VN reinforced PM HSS was prepared from water atomised powders via pressureless sintering. The main conclusions are as follows:

(1) Fine raw powder was employed to prepare HSS with above 98% of theoretical density. When sintered under nitrogen, a carbon–nitrogen balance state was essential to obtain the M_6C/VN reinforced HSS.

(2) Better comprehensive mechanical properties were obtained in the NM30-2 sample containing 1.0 wt.% C. The hardness, bend strength and impact energy were 65 HRC, 3011 MPa and 18–22 J, respectively.

(3) Homogenous microstructure was obtained with fine M_6C and ultrafine VN uniformly distributed in the matrix. The average grain size of VN was 0.5 μm, which was much smaller than VC, resulting in the enhancement of mechanical performance.

(4) The formation mechanism was elucidated. The standard Gibbs free energy of VN was much lower than the VC phase. Besides, the formation energy of VN was −9.45 eV, while that of VC was −9.08 eV.

Disclosure statement

No potential conflict of interest was reported by the authors.

Funding

This work was supported by the China Postdoctoral Research Foundation [No. 2018M641188] and the Fundamental Research Funds for the Central Universities [No. FRF-TP-18-025A1].

Notes on contributors

Haixia Sun is Ph.D. candidate in Engineering at the University of Science and Technology Beijing. She is engaged in the researches on powder metallurgy iron-based materials.

Fang Yang is a Ph.D. in Engineering and works as a lecturer at the University of Science and Technology Beijing. Her research interests include powder metallurgy titanium and titanium alloys, aluminum and aluminum alloys, copper and copper alloys, 3D printing, iron-based alloys, self-propagating high temperature synthesis (SHS), and magnetic materials.

Qian Qin is Ph.D. candidate in Engineering at the University of Science and Technology Beijing. He is engaged in the researches on powder metallurgy iron-based materials.

Biao Zhang is a master in Engineering graduated from the University of Science and Technology Beijing. He is engaged in the researches on powder metallurgy iron-based materials.

Alex A. Volinsky is an Associate Professor at the University of South Florida, USA. He is an expert in thin films processing, mechanical properties and characterization, adhesion and fracture of thin films, nanoindentation, pattern formation, irradiated materials properties and X-Ray diffraction.

Zhimeng Guo is a Professor and Ph.D. supervisor working at the University of Science and Technology Beijing. He offers courses in Powder Metallurgy. He is an expert in powder metallurgy titanium and titanium alloys, aluminum and aluminum alloys, copper and copper alloys, 3D printing, iron-based alloys, dispersion strengthened materials, radio frequency inductively coupled plasma spheroidization technology, self-propagating high temperature synthesis (SHS), advanced powder metallurgy technologies and materials.

ORCID

Alex A. Volinsky http://orcid.org/0000-0002-8520-6248

References

[1] Mesquita RA, Barbosa CA. High-speed steels produced by conventional casting, spray forming and powder metallurgy. Mater Sci Forum. 2005;498–499:244–250.

[2] Sustarsic B, Kosec L, Jenko M, et al. Vacuum sintering of water-atomised HSS powders with MoS_2 additions. Vacuum. 2001;61:471–477.

[3] Sustarsic B, Kosec L, Kosec M, et al. The influence of MoS_2 additions on the densification of water-atomized HSS powders. J Mater Process Technol. 2006;173:291–300.

[4] Škapin SD, Jenko M, Leskovšek V, et al. Characterization of the carbides and the martensite phase in powder-metallurgy high-speed steel. Mater Charact. 2010;61:452–458.

[5] Zhang X, Liu W, Sun D, et al. The transformation of carbides during austenization and its effect on the wear resistance of high speed steel rolls. Metall Mater Trans A. 2007;38:499–505.

[6] Ding P, Shi G, Zhou S. As-cast carbides in high-speed steels. Metall Mater Trans A. 1993;24:1265–1272.

[7] Zhang L, Zhang X, Li L, et al. Evolution of the microstructure and mechanical properties of powder metallurgical high-speed steel S390 after heat treatment. J Alloys Compd. 2017;740:766–773.

[8] Grinder O. The HIP way to make cleaner, better steels. Met Powder Rep. 2007;62:16-18.

[9] Wright CS, Ogel B. Supersolidus sintering of high speed steels: part 1: sintering of molybdenum based alloys. Powder Metall. 1993;36:213–219.

[10] Wright CS, Ogel B, Lemoisson F, et al. Supersolidus sintering of high speed steels: part 2: sintering of tungsten based alloys. Powder Metall. 1995;38:221–229.

[11] Zhang D, Li Z, Xie L, et al. Powder metallurgy of high speed-steel produced by solid state sintering and heat treatment. Int J Mater Res. 2015;106:870–876.

[12] Zhang QK, Jiang Y, Shen WJ, et al. Direct fabrication of high-performance high speed steel products enhanced by LaB_6. Mater Des. 2016;112:469–478.

[13] Giménez S, Zubizarreta C, Trabadelo V, et al. Sintering behaviour and microstructure development of T42 powder metallurgy high speed steel under different processing conditions. Mater Sci Eng A. 2008;480:130–137.

[14] Aguirre I, Gimenez S, Talacchia S, et al. Effect of nitrogen on supersolidus sintering of modified M35M high speed steel. Powder Metall. 1999;42:353–357.

[15] Bolton JD, Gant AJ. Fracture in ceramic-reinforced metal matrix composites based on high-speed steel. J Mater Sci. 1998;33(4):939–953.

[16] Bolton JD, Gant AJ. Microstructural development and sintering kinetics in ceramic reinforced high speed steel metal matrix composites. Powder Metall. 1997;40(2):143–151.

[17] Gordo E, Velasco F, Antón N, et al. Wear mechanisms in high speed steel reinforced with $(NbC)_p$ and $(TaC)_p$ MMCs. Wear. 2000;239(2):251–259.

[18] Pines ML, Bruck HA. Pressureless sintering of particle-reinforced metal-ceramic composites for functionally graded materials: part I. Porosity reduction models. Acta Mater. 2006;54:1457–1465.

[19] Chamberlain AL, Fahrenholtz WG, Hilmas GE. Pressureless sintering of zirconium diboride. J Am Ceram Soc. 2006;89:450–456.

[20] Kim HC, Oh DY, Shon IJ. Sintering of nanophase WC-15vol.%Co hard metals by rapid sintering process. Int J Refract Met Hard Mater. 2004;22:197–203.

[21] Trabadelo V, Giménez S, Iturriza I. Microstructural characterisation of vacuum sintered T42 powder metallurgy high-speed steel after heat treatments. Mater Sci Eng A. 2009;499:360–367.

[22] Godec M, Večko Pirtovšek T, Šetina Batič B, et al. Surface and bulk carbide transformations in high-speed steel. Sci Rep. 2015;5:1–11.

[23] Gimenez S, Iturriza I. Microstructural characterisation of powder metallurgy M35MHV HSS as a function of the processing route. J Mater Process Technol. 2003;143–144:555–560.

[24] Xu HX, Zhu WL, Jiang JQ, et al. Refining carbide dimensions in AISI M2 high speed steel by increasing solidification rates and spheroidising heat treatment. J Mater Sci Technol. 2013;30:116–122.

[25] Hetzner DW. Refining carbide size distributions in M1 high speed steel by processing and alloying. Mater Charact. 2001;46:175–182.

[26] Huang PY. Powder metallurgy. Beijing: Metallurgical Industry Press; 1997.

[27] Gan Y. Iron and steel materials engineering. Beijing: Chemical Industry press; 2005.

[28] Gomes MA, Wronski AS, Wright CS. Fracture behaviour of a highly alloyed high speed steel. Fatigue Fract Eng M. 2007;18(1):1–18.